Supporting Information

π-Adsorption Promoted Electrocatalytic Acetylene Semihydrogenation on Single-Atom Ni Dispersed N-doped Carbon

Wenxiu Ma[†a], Zhe Chen[†b], Jun Bu[a], Zhenpeng Liu[a], Jinjin Li[a], Chen Yan[a], Lin Cheng[d], Lei Zhang[a], Hepeng Zhang[a], Jichao Zhang[c]*, Tao Wang[b]*, and Jian Zhang[a]*

a. Key Laboratory of Special Functional and Smart Polymer Materials of Ministry of Industry and Information Technology, School of Chemistry and Chemical Engineering, Northwestern Polytechnical University, Xi' an, 710129, P. R. China.
   Email: zhangjian@nwpu.edu.cn
b. Center of Artificial Photosynthesis for Solar Fuels, School of Science, Westlake University, Hangzhou 310024, P. R. China.
   Email: twang@westlak.edu.cn.
c. Shanghai Synchrotron Radiation Facility, Zhangjiang Laboratory, Shanghai Advanced Research Institute, Chinese Academy of Sciences, Shanghai, 201204, P. R. China.
   Email: zhangjichao@zjlab.org.cn
d. School of Science, Xi'an Polytechnic University, Xi'an, 710048, P. R. China.

[†]These authors contributed equally to this work.

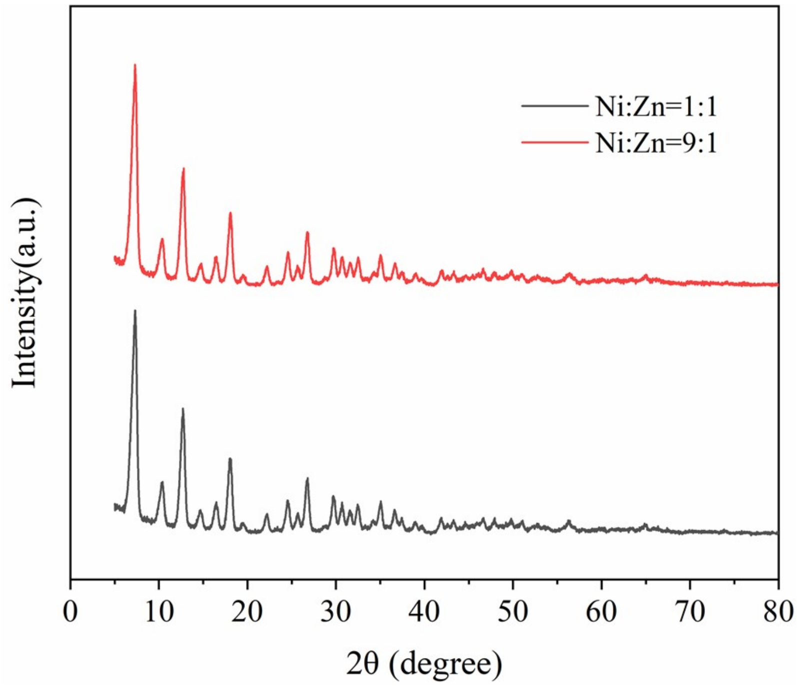

Figure S1. XRD pattern of ZnNi ZIF precursor from two different metal concentrations.

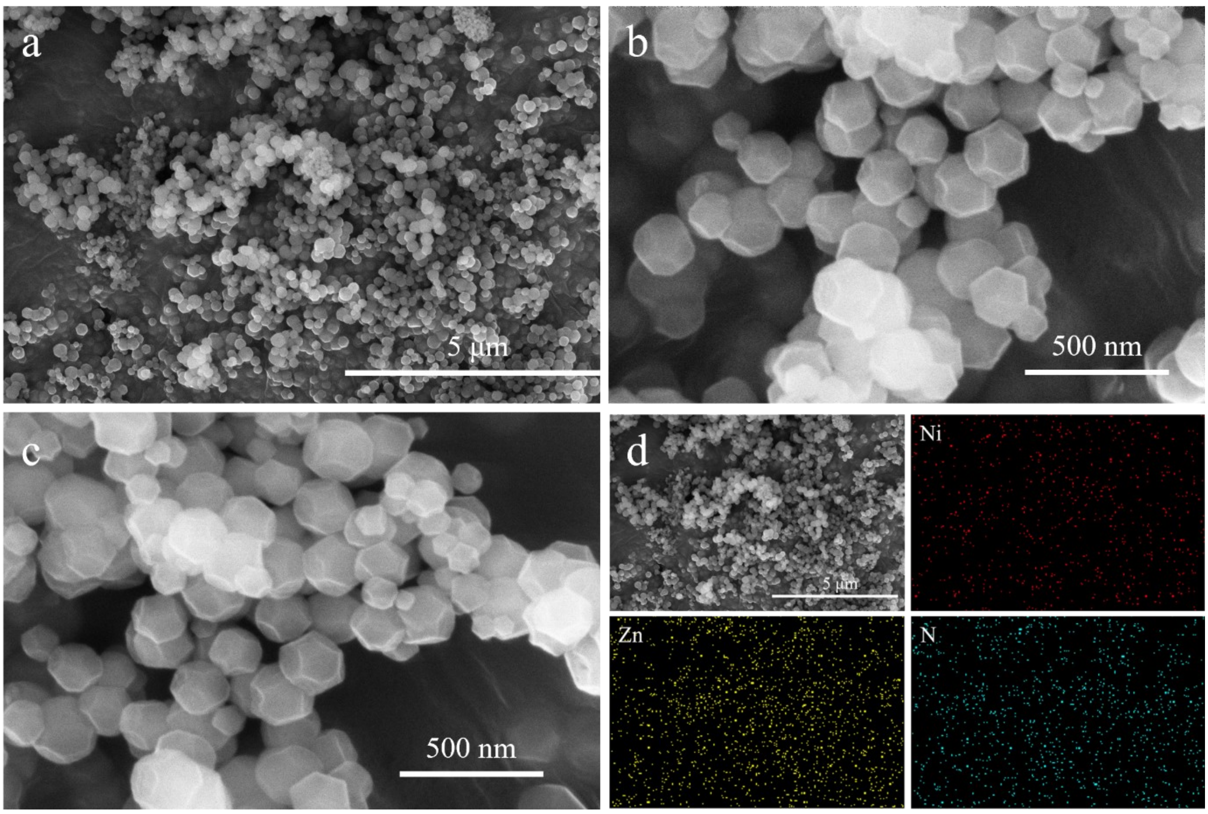

Figure S2. a-c, SEM images of ZnNi ZIF precursor (Ni:Zn=1:1). d, Corresponding elemental mapping images of Ni, Zn, and N.

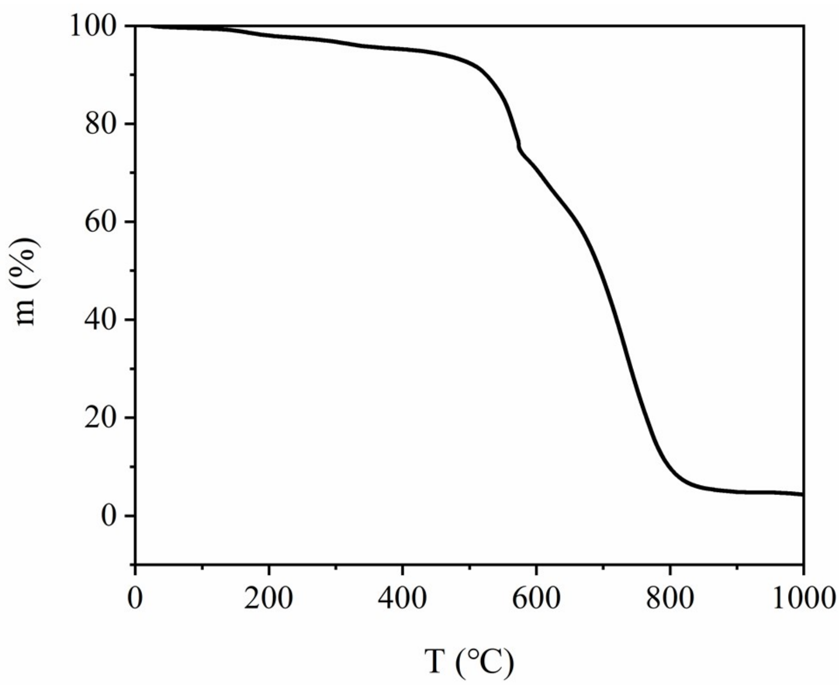

Figure S3. TGA pattern of ZnNi-ZIF.

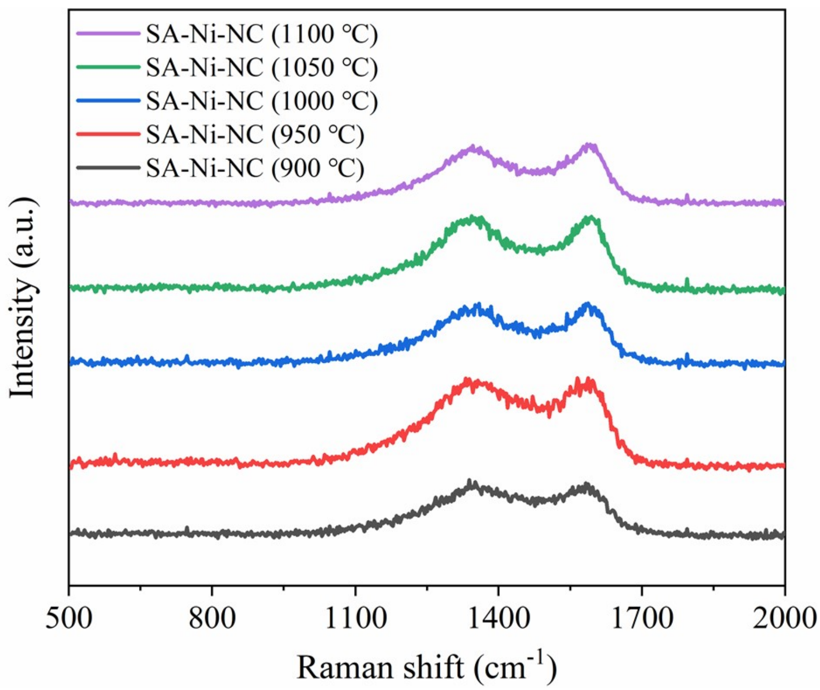

Figure S4. Raman spectra of SA-Ni-NC prepared at different heating treatment.

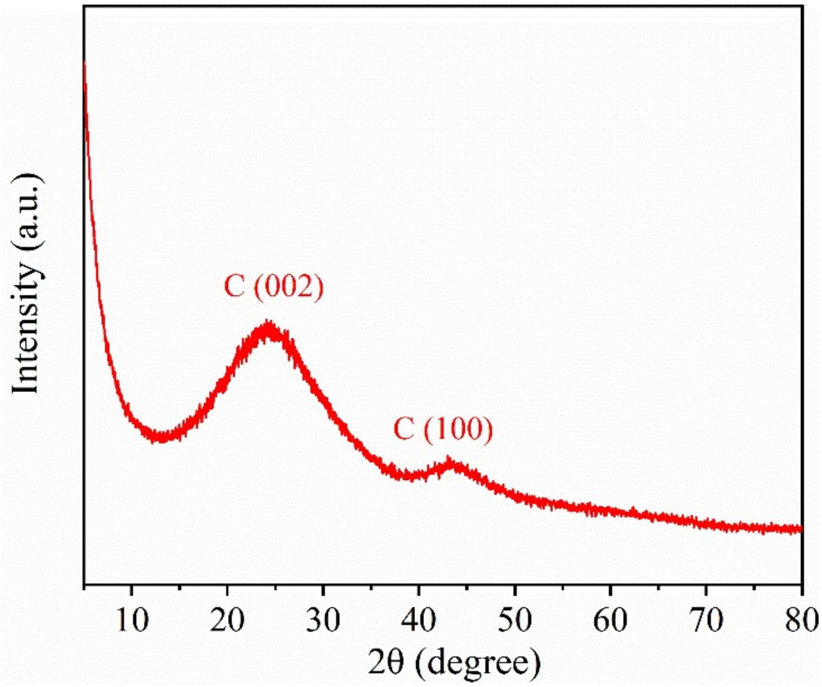

Figure S5. XRD pattern of SA-Ni-NC pyrolyzed at 950 °C.

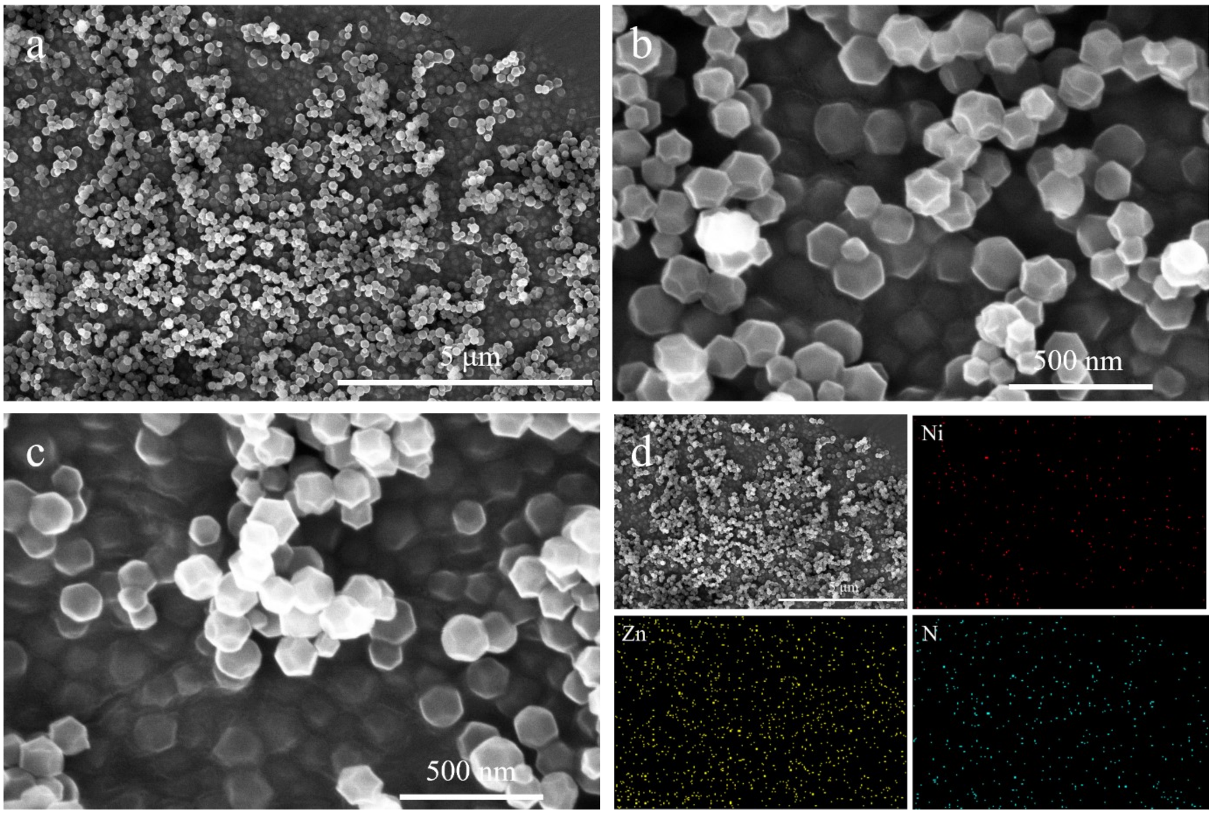

Figure S6. a-c, SEM images of ZnNi ZIF precursor (Ni:Zn=9:1). d, Corresponding elemental mapping images of Ni, Zn, and N.

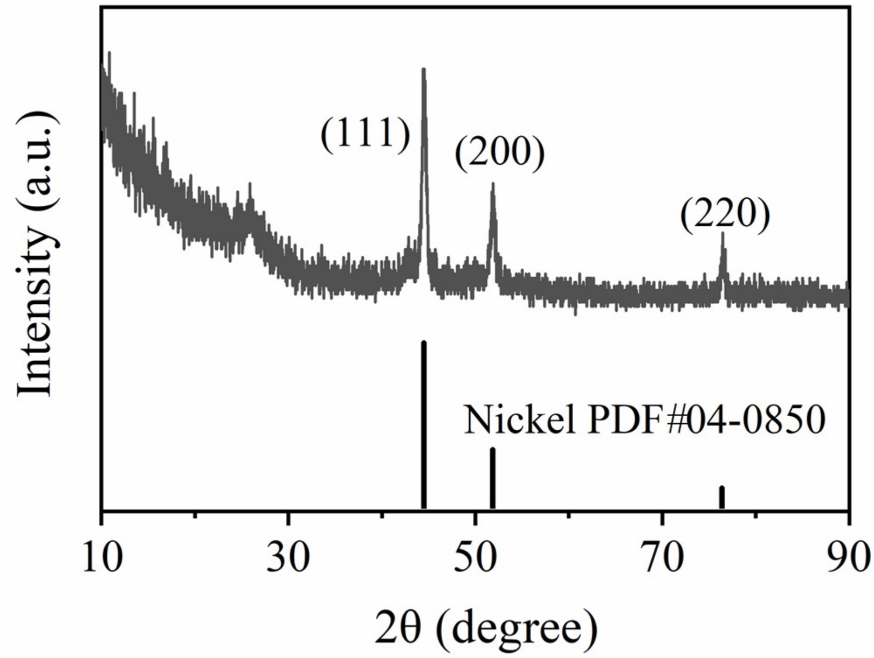

Figure S7. XRD pattern of Ni NP/N-C pyrolyzed at 950 °C.

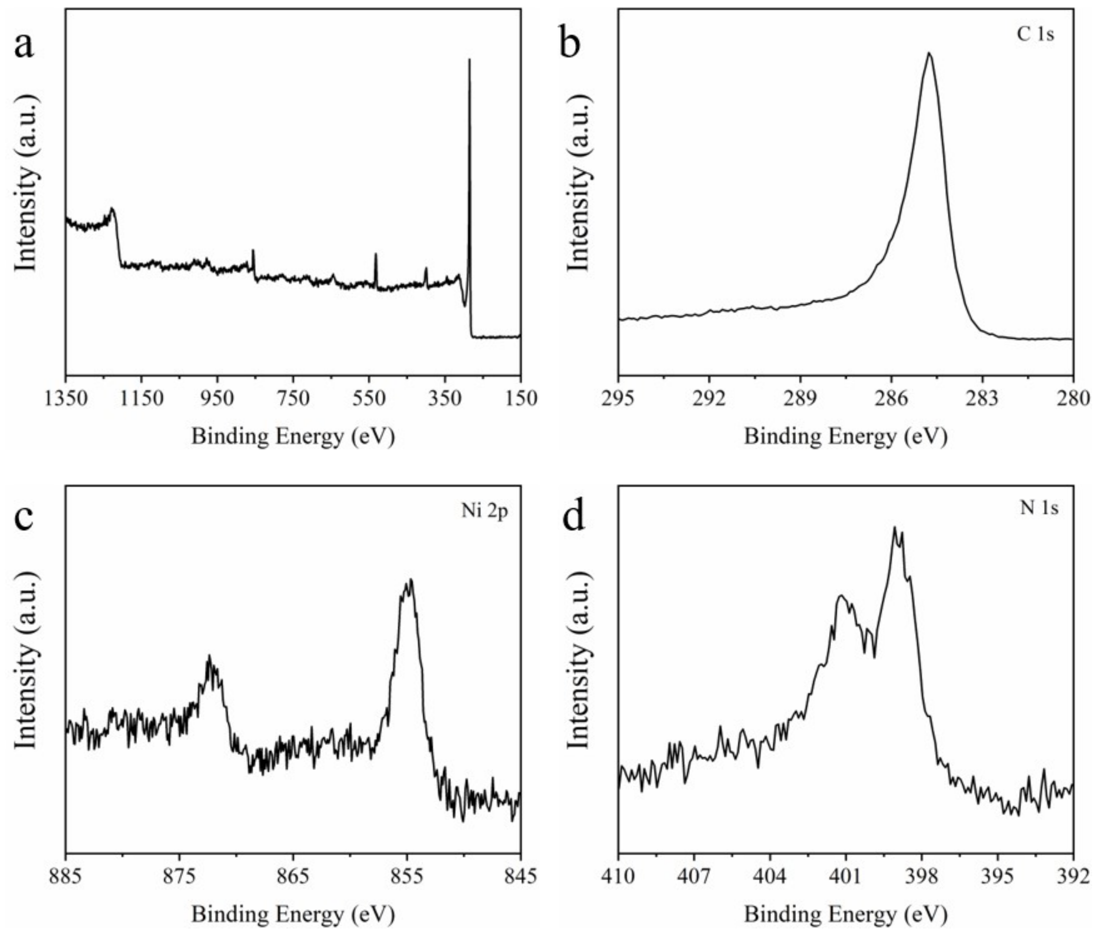

Figure S8. XPS spectra for Ni NP/N-C. a, Survey curve, b, C 1s, c, Ni 2p, and d, N 1s spectra of Ni NP/N-C.

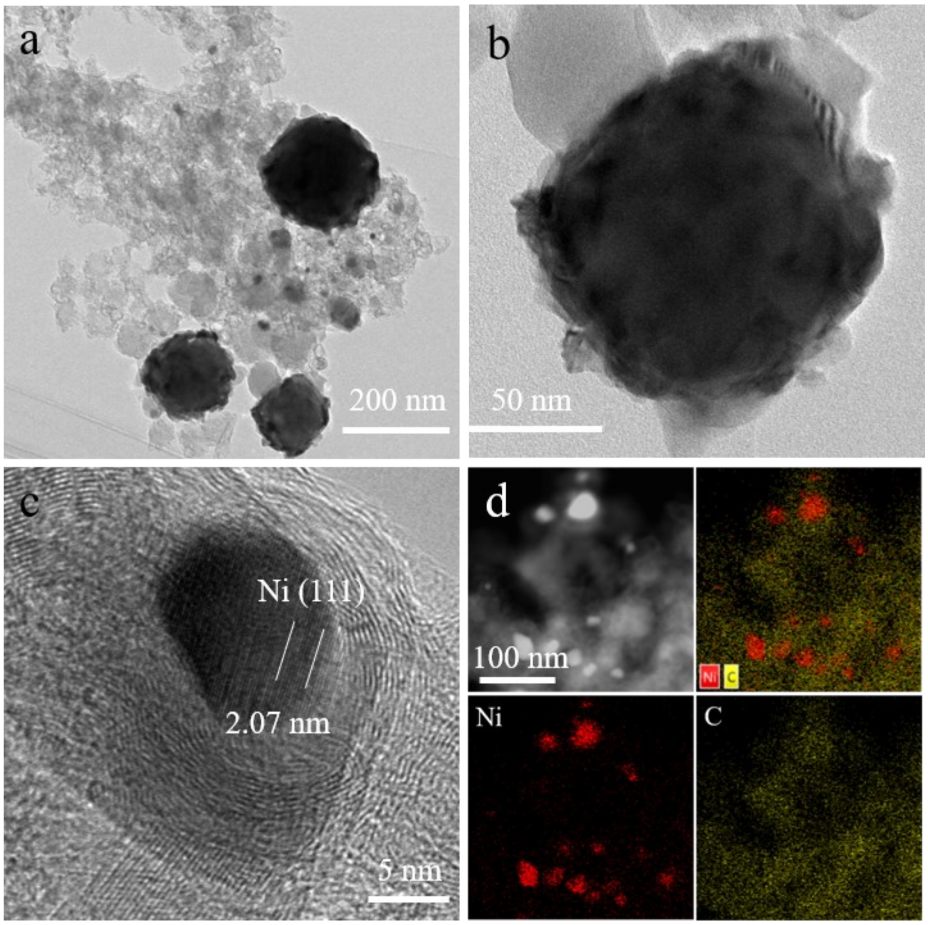

Figure S9. a-b, TEM images of Ni NP/N-C. c, HRTEM images of Ni NP/N-C. d, HAADF-STEM image of Ni NP/N-C and corresponding elemental mapping images of C and Ni.

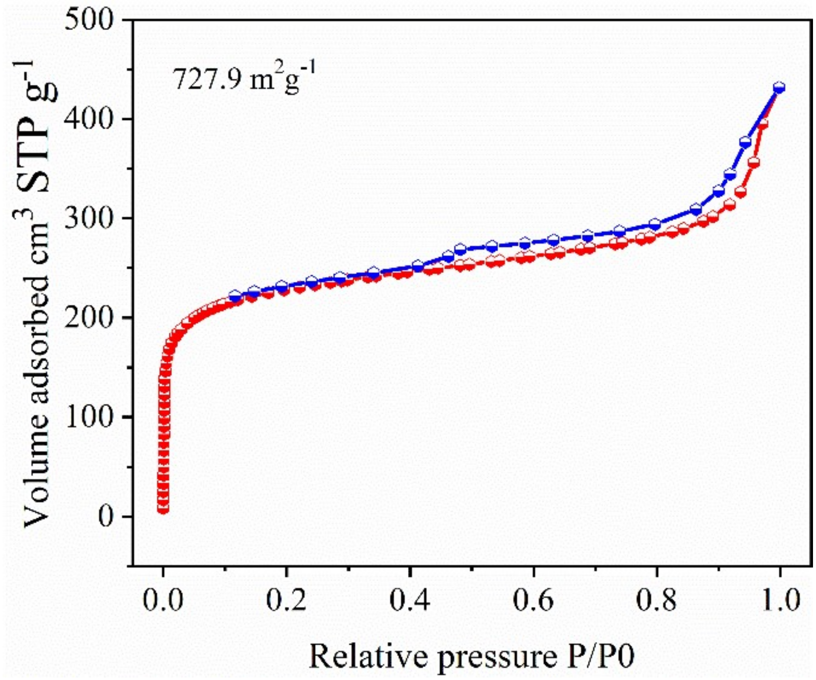

Figure S10. BET adsorption/desorption isotherms of SA-Ni-NC.

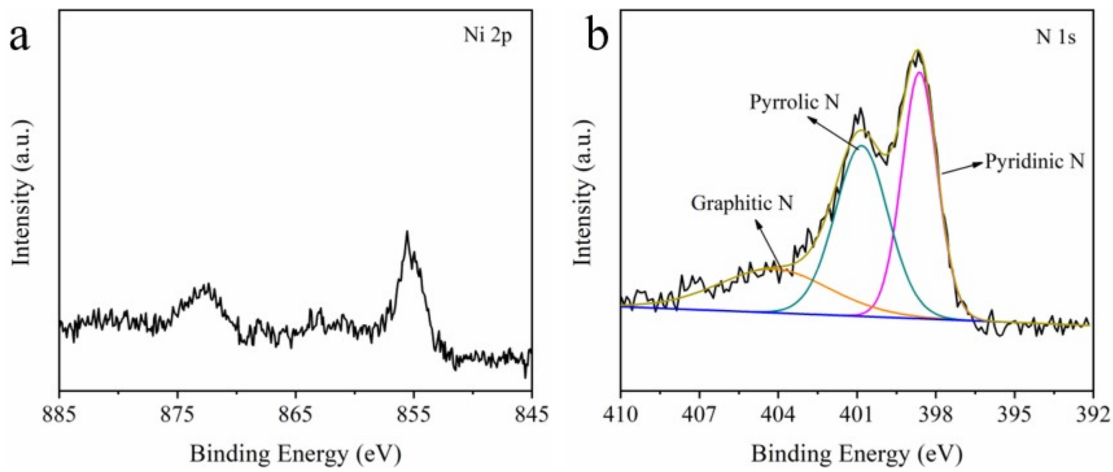

Figure S11. XPS spectra for the a, Ni 2p, b, N 1s of SA-Ni-NC.

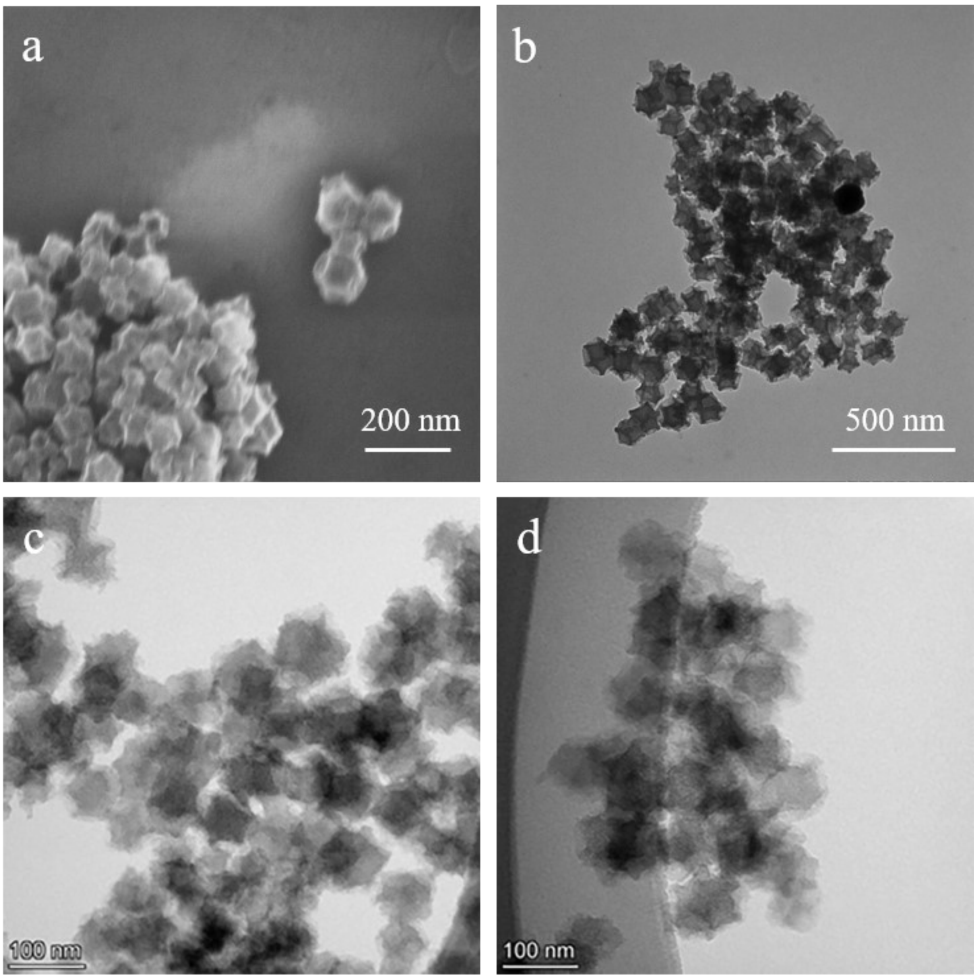

Figure S12. a, SEM and b-d, TEM images of SA-Ni-NC.

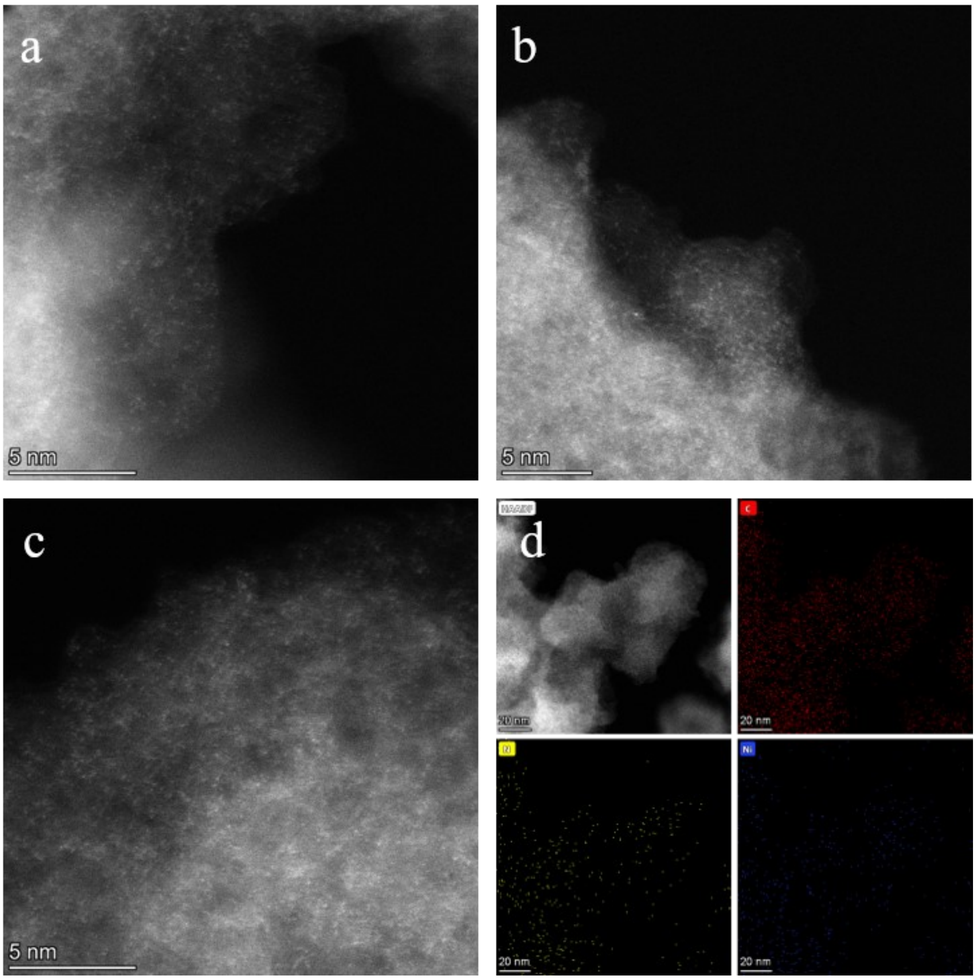

Figure S13. a-c, HRTEM images of SA-Ni-NC. d, HAADF-STEM image of SA-Ni-NC and corresponding elemental mapping images of C, N, and Ni.

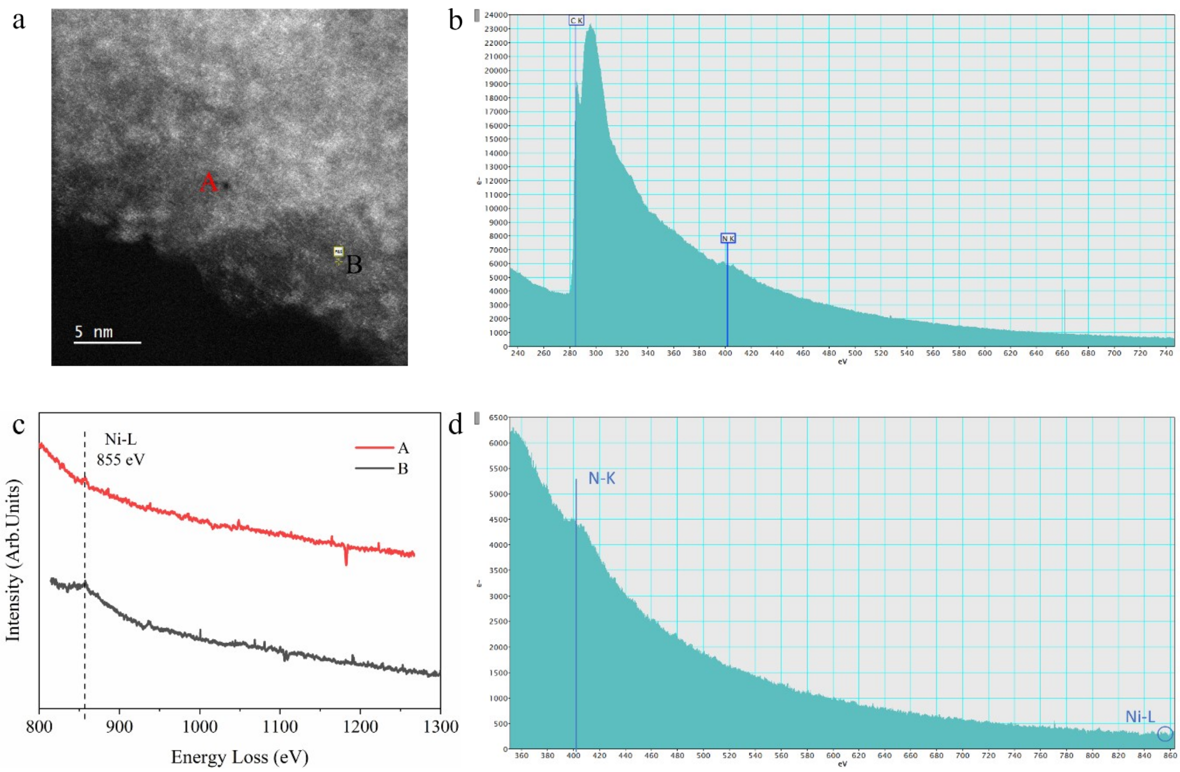

Figure S14. Atomically resolved EELS identification of a single Ni. a, HAADF image displaying atomic resolution. b-d, selection of EELS within a different range. Red and black spectra in c correspond to the pixels outlined in A and B points in a.

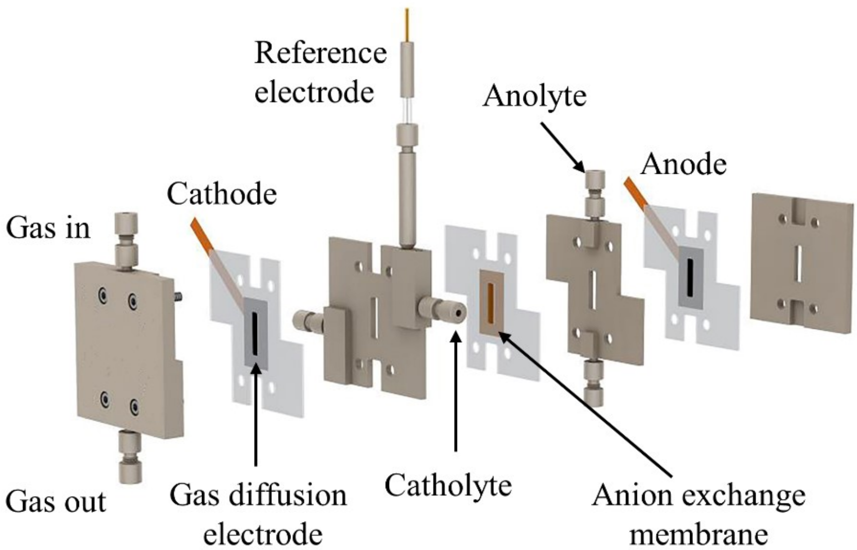

Figure S15. Graphic illustration for a flow cell.

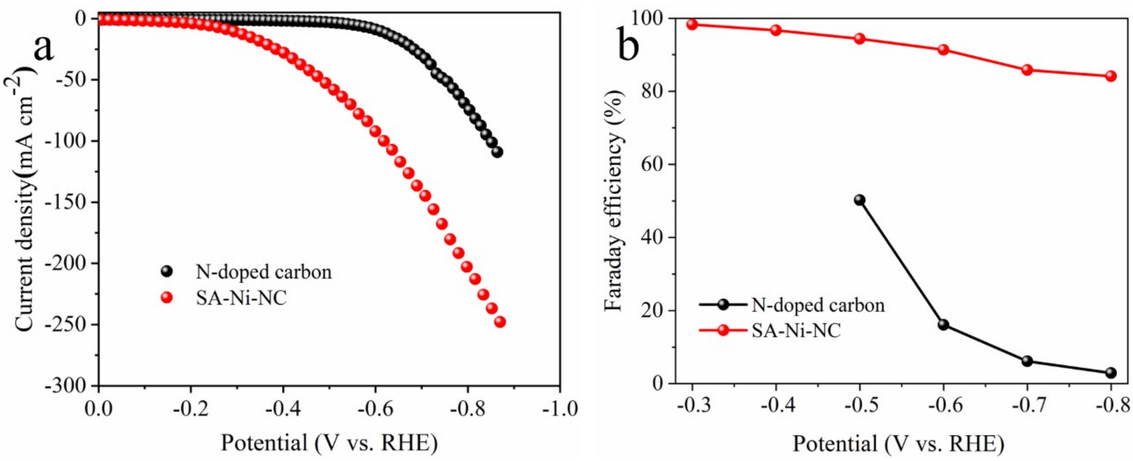

Figure S16. Electrocatalytic performance of N-doped carbon and SA-Ni-NC under pure acetylene flow. a, LSV curves at a scan rate of 5 mV s^{-1}. b, Faradaic efficiencies of C_2H_4.

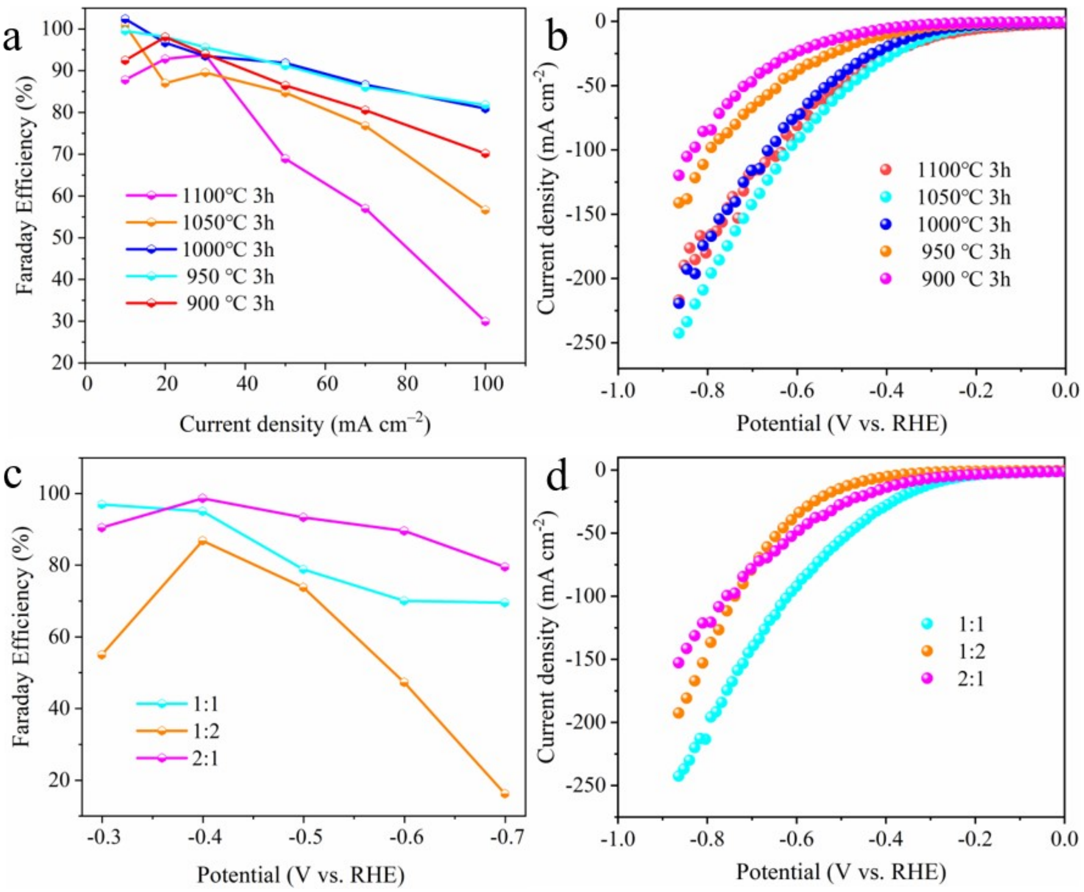

Figure S17. a, Ethylene Faradaic efficiency and b, LSV curves of catalyst prepared at different heating temperatures. c, Ethylene Faradaic efficiency and d, LSV curves of catalyst prepared at different ratios of Ni and Zn.

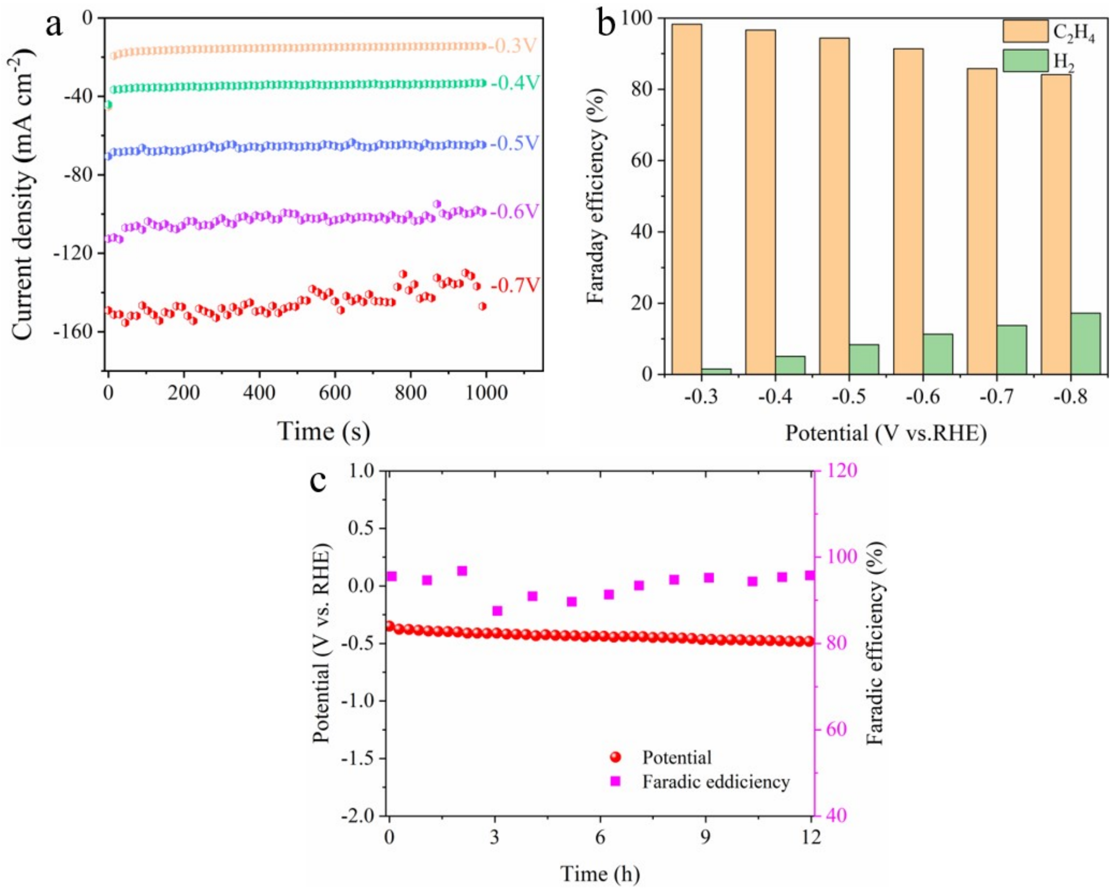

Figure S18. Electrochemical carbon dioxide reduction measurements in a three-electrode flow cell. a, Chronoamperometric plots of SA-Ni-NC at different potentials. b, Faradaic efficiency of ethylene and H_2 for SA-Ni-NC. c, Long-term stability test of SA-Ni-NC at a current density of -30 mA cm^{-2}.

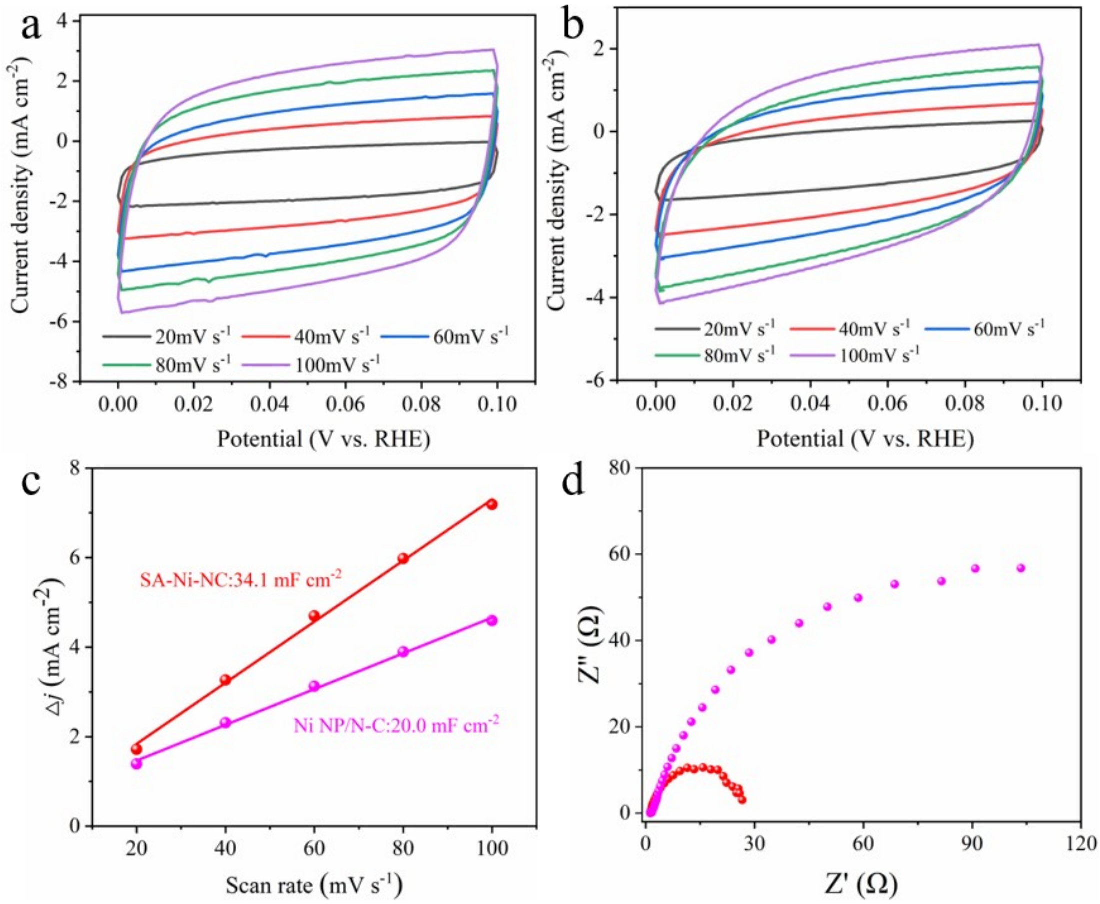

Figure S19. Electrochemical capacitance and electrochemical impedance spectroscopy (EIS) measurements. a-b, Cyclic voltammogram (CV) curves were recorded in a potential range (0.00~0.1 V) without faradic processes for SA-Ni-NC and Ni NP/N-C. c, The linear slopes of is equivalent to twice of the double-layer capacitance C_{dl}, and the C_{dl} is proportional to the ECSA. d, EIS of SA-Ni-NC and Ni NP/N-C in the frequency range of 0.01 to 10^5 Hz.

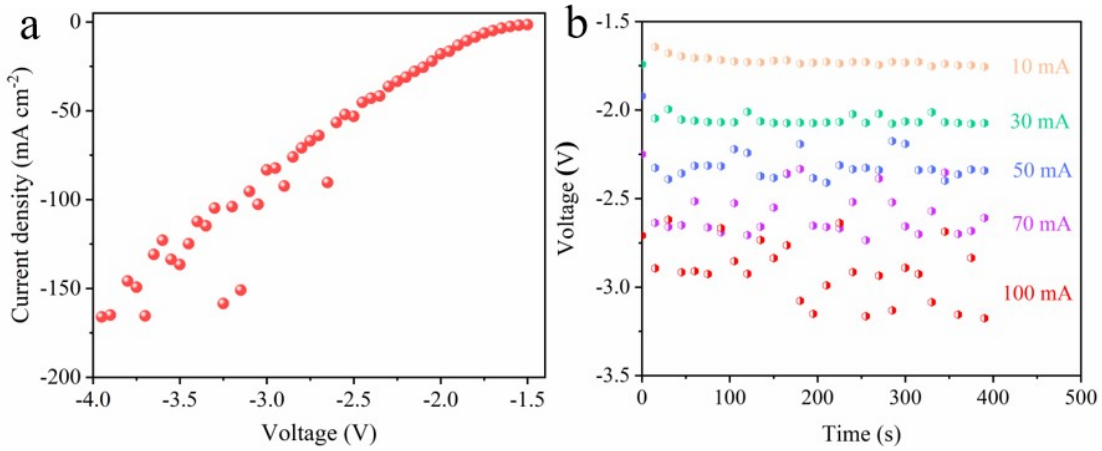

Figure S20. Electrochemical performance of the full cell based on the SA-Ni-NC/NiFe-LDH pair. a, LSV curve in acetylene at a scan rate of 1 mV s^{-1}. b, Chronoamperometric responses of at different voltages.

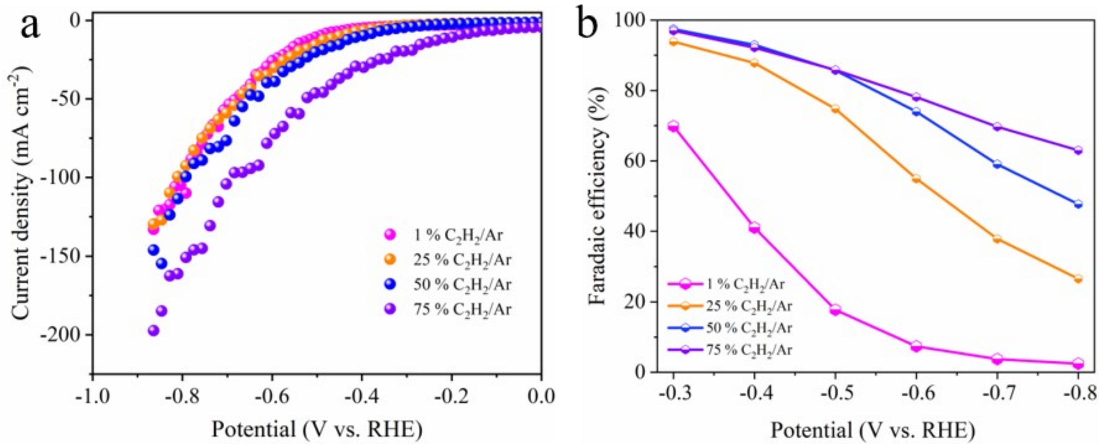

Figure S21. a, LSV curves of SA-Ni-NC in 1 M KOH aqueous solution under acetylene flow with different concentrations. b, $FE_{ethylene}$ of SA-Ni-NC at different potentials.

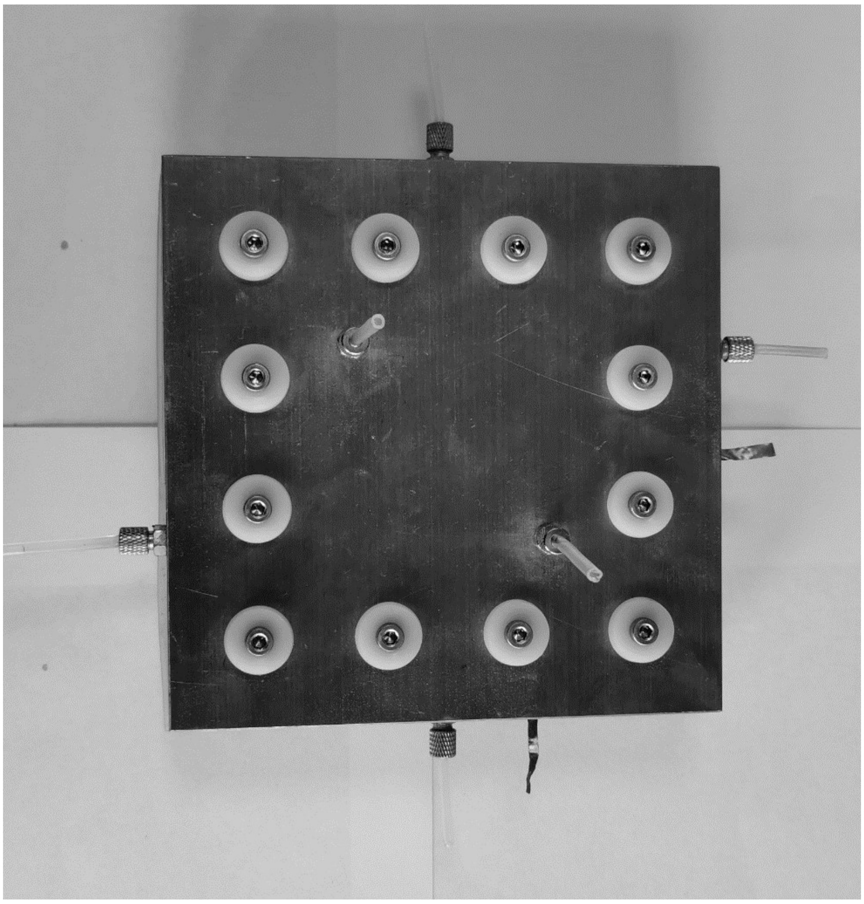

Figure S22. Digital images of the as-designed flow cell with an electrode area of 25 cm^2.

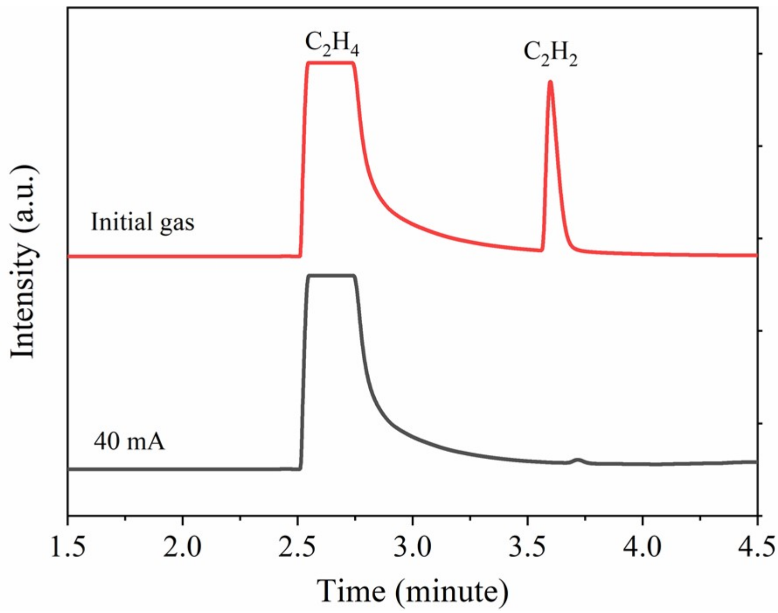

Figure S23. Gas chromatography curves of electrocatalytic acetylene semihydrogenation on SA-Ni-NC catalyst at a flow rate of 10 sccm.

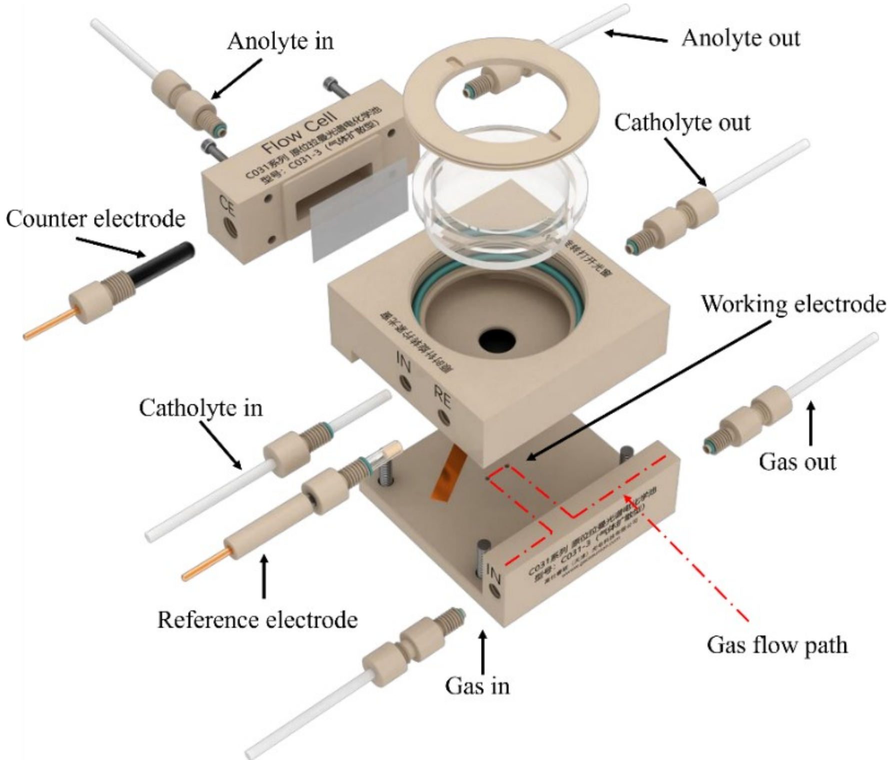

Figure S24. Graphic illustration of the flow cell for in situ Raman spectroscopy.

The flow cell for in-situ Raman spectroscopy is provided by GaossUnion (Tian Jin) Photoelectric technology. The gas-diffusion carbon papers loaded with electrocatalysts (1 mg cm^{-2}) served as the working electrode. Ag/AgCl electrode and graphite rod were used as the reference and counter electrodes, respectively. 1 M KOH aqueous solution at a flow rate of 10 ml min^{-1} were utilized as electrolytes at both cathode and anode chambers. An anion exchange membrane was sandwiched between catholyte and anolyte compartments to avoid product crossover. The C_2H_2/Ar (50 %/50 %) flow was fed to the cathode at 20 ml min^{-1} using a mass flow controller.

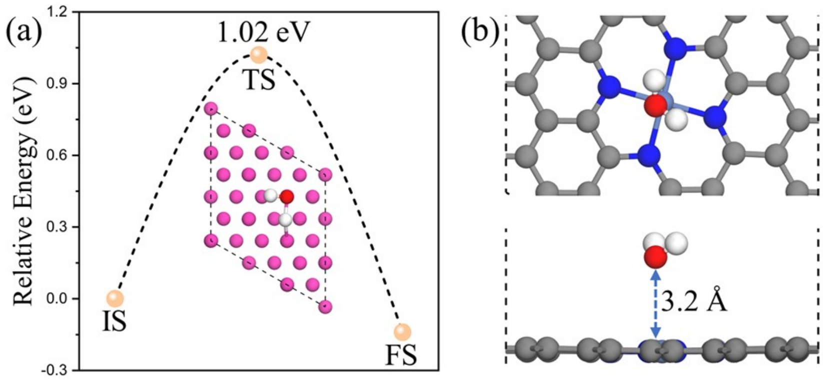

Figure S25. (a) the free energy diagram for water dissociation on the Ni NP/NC (111) surface. (b) the adsorption configuration of water on the SA-Ni-NC catalyst.

Table S1. Loading weight of Ni in SA-Ni-NC determined by ICP

Sample	Ni loading (wt.%)
SA-Ni-NC-1	2.3482
SA-Ni-NC-2	2.4455

Table S2. XAFS data fitting results of SA-Ni-NC.

Sample	Shell	N	R (Å)	σ2 (Å2)	ΔE0 (eV)	R factor
Ni foil	Ni-Ni 1st shell	12 (fixed)	2.4868	0.0064	6.64	0.006
	Ni-Ni 2nd shell	6 (fixed)	3.5204	0.0100		
SA-Ni-NC	Ni-N	3.76	1.8259	0.0040	4.46	0.019

N, corrdination number; R, the distance between absorber and backscatter atoms; σ^2, the Debye-Waller factor value; E_0 (eV), inner potential correction to account for the difference in the inner potential between the sample and the reference compound.

Table S3. The acetylene semihydrogenation performances of reported thermocatalyst and this work.

Catalyst	Gas composition	Temperature (°C)	space velocity (mL·g_{cat}^{-1}·h^{-1})	C_2H_2 conversion (%)	C_2H_4 selectivity (%)
SA-Ni-NC (This work)	**C_2H_2/C_2H_4 =1/99**	**25**	**2.4×10^4**	**97.4**	**>99.9**
Fe^{III}-ZrO_2[1]	C_2H_2/C_2H_4 =1.2/98.8	100	4.0×10^3	>99	87.5
Pd/PPS[2]	$C_2H_2/C_2H_4/H_2/C_3H_8/N_2$ =0.6/49.3/0.9/0.6/48.6	100	1.637×10^3	45.0	78.0
Pd/$Ni(OH)_2$[3]	$C_2H_2/C_2H_4/H_2$/He =0.65/50/5/44.35	105	2.4×10^4	73.0	79.0
Grapheme[4]	$C_2H_2/C_2H_4/H_2$ =2.5/22.5/75	110	1.46×10^4	81.0	92.2
Pt/TiWN[5]	C_2H_2/ H_2/CH_4/He= 5/20/8/67	115	1.8×10^3	78.0	77.0
ISA-Pd/MPNC[6]	$C_2H_2/C_2H_4/H_2$/He =0.5/50/5/44.5	120	1.05×10^4	85.0	82.0
Pd-SAs-900[7]	$C_2H_2/C_2H_4/H_2$/He= 0.5/50/5/44.5	120	1.2×10^3	96.0	93.4
Pd_2Sn/C[8]	mixture of C_2H_2, C_2H_4 and H_2	160	8.0×10^3	100.0	93.0
$Co_2Mn_{0.5}Fe_{0.5}Ge$[9]	$C_2H_2/C_2H_4/H_2$/He =0.1/10/40/49.9	170	2.0×10^4	63.5	85.0
Cu/Al_2O_3 SAC[10]	$C_2H_2/C_2H_4/H_2$/Ar =1/50/10/39	178	8×10^3	76.0	91.0
Na-Ni@CHA[11]	C_2H_2/H_2/He= 1/16/83	180	1.5×10^4	100.0	97.0
In_2O_3 nanopowder[12]	C_2H_2/H_2=3.23/96.77	180	2.0966×10^4	66.0	85.0
Cu_1/ND@G[13]	$C_2H_2/C_2H_4/H_2$/He= 1/20/10/69	200	3.0×10^3	95.0	98.0

Reference

1. M. Tejeda-Serrano, M. Mon, B. Ross, F. Gonell, J. s. Ferrando-Soria, A. Corma, A. Leyva-Pérez, D. Armentano and E. Pardo, *J. Am. Chem. Soc.*, 2018, **140**, 8827-8832.
2. S. Lee, S.-J. Shin, H. Baek, Y. Choi, K. Hyun, M. Seo, K. Kim, D.-Y. Koh, H. Kim and M. Choi, *Sci. adv.*, 2020, **6**, eabb7369.
3. M. Hu, J. Zhang, W. Zhu, Z. Chen, X. Gao, X. Du, J. Wan, K. Zhou, C. Chen and Y. Li, *Nano Res.*, 2018, **11**, 905-912.
4. A. Primo, F. Neatu, M. Florea, V. Parvulescu and H. Garcia, *Nat. commun.*, 2014, **5**, 1-9.
5. Z. Wang, A. Garg, L. Wang, H. He, A. Dasgupta, D. Zanchet, M. J. Janik, R. M. Rioux and Y. Román-Leshkov, *ACS Catal.*, 2020, **10**, 6763-6770.
6. Q. Feng, S. Zhao, Q. Xu, W. Chen, S. Tian, Y. Wang, W. Yan, J. Luo, D. Wang and Y. Li, *Adv. Mater.*, 2019, **31**, 1901024.
7. S. Wei, A. Li, J.-C. Liu, Z. Li, W. Chen, Y. Gong, Q. Zhang, W.-C. Cheong, Y. Wang and L. Zheng, *Nat. nanotechnol.*, 2018, **13**, 856-861.
8. R. Li, Y. Yue, Z. Chen, X. Chen, S. Wang, Z. Jiang, B. Wang, Q. Xu, D. Han and J. Zhao, *Appl. Catal., B*, 2020, **279**, 119348.
9. T. Kojima, S. Kameoka, S. Fujii, S. Ueda and A.-P. Tsai, *Sci. adv.*, 2018, **4**, eaat6063.
10. X. Shi, Y. Lin, L. Huang, Z. Sun, Y. Yang, X. Zhou, E. Vovk, X. Liu, X. Huang and M. Sun, *ACS Catal.*, 2020, **10**, 3495-3504.
11. Y. Chai, G. Wu, X. Liu, Y. Ren, W. Dai, C. Wang, Z. Xie, N. Guan and L. Li, *J. Am. Chem. Soc.*, 2019, **141**, 9920-9927.
12. D. Albani, M. Capdevila-Cortada, G. Vilé, S. Mitchell, O. Martin, N. López and J.

Pérez-Ramírez, *Angew. Chem., Int. Ed.*, 2017, **129**, 10895-10900.

13. F. Huang, Y. Deng, Y. Chen, X. Cai, M. Peng, Z. Jia, J. Xie, D. Xiao, X. Wen and N. Wang, *Nat. commun.*, 2019, **10**, 1-7.